Draft version May 19, 2016
Preprint typeset using LaTeX style emulateapj v. 5/2/11

arXiv:1605.05373v1 [astro-ph.CO] 17 May 2016

BINARY BLACK HOLES, GAS SLOSHING, AND COLD FRONTS IN THE X-RAY HALO HOSTING 4C+37.11

Felipe Andrade-Santos[1], Ákos Bogdán[1], Roger W. Romani[2], William R. Forman[1], Christine Jones[1], Stephen S. Murray[1], Greg B. Taylor[3], and Robert T. Zavala[4]

[1]Harvard-Smithsonian Center for Astrophysics, 60 Garden Street, Cambridge, MA 02138, USA
[2]Department of Physics, Stanford University, Stanford, CA 94305-4060, USA
[3]Department of Physics and Astronomy, University of New Mexico, Albuquerque, NM 87131, USA
[4]US Naval Observatory, Flagstaff Station, 10391 W. Naval Observatory Rd, Flagstaff, AZ 86001, USA

Draft version May 19, 2016

ABSTRACT

We analyzed deep *Chandra* ACIS-I exposures of the cluster-scale X-ray halo surrounding the radio source 4C+37.11. This remarkable system hosts the closest resolved pair of super-massive black hole and an exceptionally luminous elliptical galaxy, the likely product of a series of past mergers. We characterize the halo with $r_{500} = 0.95$ Mpc, $M_{500} = (2.5 \pm 0.2) \times 10^{14}\ M_{\odot}$, $kT = 4.6 \pm 0.2$ keV, and a gas mass of $M_{\rm g,500} = (2.2 \pm 0.1) \times 10^{13} M_{\odot}$. The gas mass fraction within r_{500} is $f_{\rm g} = 0.09 \pm 0.01$. The entropy profile shows large non-gravitational heating in the central regions. We see several surface brightness jumps, associated with substantial temperature and density changes, but approximate pressure equilibrium, implying that these are sloshing structures driven by a recent merger. A residual intensity image shows core spiral structure closely matching that seen for the Perseus cluster, although at $z = 0.055$ the spiral pattern is less distinct. We infer the most recent merger occurred $1 - 2$ Gyr ago and that the event that brought the two observed super-massive black holes to the system core is even older. Under that interpretation, this black hole binary pair has, unusually, remained at pc-scale separation for more than 2 Gyr.

Subject headings: galaxy clusters: general — cosmology: large-structure formation

1. INTRODUCTION

Supermassive Black Hole Binaries (SMBHBs) likely form through galaxy mergers (Begelman et al. 1980) and show a wide range of separations (Owen et al. 1985; Komossa et al. 2003). Recently Yan et al. (2015) suggested that a supermassive black hole binary with subparsec separation could explain the optical-UV spectrum of the quasar Mrk 231. Currently the SMBHB with the smallest directly measured projected separation (7.3 pc) lies in the core of the radio galaxy 4C+37.11 (Rodriguez et al. 2006). Through VLBA observations, Maness et al. (2004) discovered the two flat spectrum variable components in this system. Through additional VLBA observations with higher angular resolution, (Rodriguez et al. 2006) concluded that the two radio sources were the nuclei of a supermassive black hole binary system. Since the massive galaxies whose merger produces SMBHBs are often at the centers of galaxy groups or clusters, one can also observe the effects of the merger on larger scales. In particular the thermodynamic signatures of the merger in the cluster gas in the form of gas sloshing can be observed for billions of years following the merger (e.g., Ascasibar & Markevitch 2006). Gas sloshing has been extensively studied both through observations (e.g., Churazov et al. 2003; Laganá et al. 2010; Paterno-Mahler et al. 2013) and simulations (e.g., Ascasibar & Markevitch 2006; ZuHone et al. 2010; Roediger et al. 2012).

We present the large-scale properties of the cluster-scale X-ray halo hosting the radio galaxy 4C+37.11. 4C+37.11 is a remarkable system for two major reasons. First, it hosts two compact radio nuclei, resolved by Very Long Baseline Array (VLBA) observations to have a 7.3 pc projected separation, one of which currently powers relativistic jets in a Compact Symmetric Object outflow (CSO) (Maness et al. 2004; Rodriguez et al. 2006). The optical host of the SMBHB is a relatively isolated, extremely luminous elliptical galaxy with M_{K_s} = -27.0, which corresponds to a stellar mass of $M_{\odot} = 9.5 \times 10^{11} M_{\odot}$. Given the environment of the system, the source may be a fossil group (Romani et al. 2014) with an unmerged pair of nuclear black holes. Second, X-ray observations of 4C+37.11 show that the binary black hole is embedded in a bright, extended X-ray halo. Specifically, the X-ray luminosity within R_{2500} = 400 kpc is $L_{\rm X} \sim 10^{44}$ erg s^{-1}. These characteristics show that 4C+37.11 resides in galaxy cluster-sized dark matter halo. Previous *Chandra* observations revealed that the hot gas shows edge structures (Romani et al. 2014), hinting at a past merger, which may have led to the formation of the observed SMBHB. However, the previous *Chandra* observation did not have sufficiently high signal-to-noise ratio to constrain the origin of the edges. The goal of this paper is to utilize our deep *Chandra* X-ray observations to probe the origin of the edge structures, and constrain the characteristics of the merger that led to the formation of a binary black hole.

The paper is structured as follows. In Section 2 we describe the data reduction. In Section 3, overall properties of the halo hosting 4C+37.11 are described. In Section 4 we present evidence of a sloshing feature in 4C+37.11. The small scale structure of the cluster is investigated in Section 5. We discuss the implications of our results in Section 6, and we conclude in Section 7.

Assuming a standard ΛCDM cosmology with $H_0 = 70$ km s^{-1} Mpc^{-1}, $\Omega_{\rm M} = 0.3$, and $\Omega_{\Lambda} = 0.7$,

the observed redshift of 4C+37.11, $z = 0.055$, implies a linear scale of 1.07 kpc arcsec^{-1} and a luminosity distance of 246 Mpc.

2. DATA REDUCTION

4C+37.11 was observed on April 4, 2011, and November 6, 2013 with the *Chandra* Observatory (both observations, the 10 ks ObsId 12704 (PI: Murray) and the 95 ks ObsId 16120 (PI: Romani) were performed with the ACIS-I array, thereby offering a large field-of-view).

The data reduction followed the process described in Vikhlinin et al. (2005). We applied the calibration files `CALDB 4.6.2`. The data reduction includes corrections for the time dependence of the charge transfer inefficiency and gain, and also a check for periods of high background (none were found). Standard blank sky background files and readout artifacts were subtracted.

3. OVERALL CHARACTERISTICS OF THE CLUSTER

3.1. *Emission measure profile*

We refer to Vikhlinin et al. (2006) for a detailed description of the procedures used to compute the emission measure profile. We outline here only the main aspects of the method.

First we detected compact sources in the 0.7–2.0 keV or 2.0–7.0 keV bands and then masked these from the spectral and spatial analyses. We then measured the surface brightness profiles in the 0.7–2.0 keV energy band, which maximizes the signal to noise ratio in *Chandra* data. The readout artifacts and blank-field background (see section 2.3.3 of Vikhlinin et al. 2006) are subtracted from the X-ray images, and the result is exposure-corrected using exposure maps (computed assuming an absorbed optically-thin thermal plasma with $kT = 5.0$ keV, abundance = 0.3 solar, plus the Galactic column density) that include corrections for bad pixels and CCD gaps, but do not take into account spatial variations of the effective area. Then, we subtract any small uniform component corresponding to soft X-ray foreground adjustments that may be required.

Following these steps, we extract the surface brightness profiles in narrow concentric annuli ($r_{\rm out}/r_{\rm in} = 1.05$) centered on the X-ray halo peak and compute the *Chandra* area-averaged effective area for each annulus (see Vikhlinin et al. 2005, for details on calculating the effective area). Using the observed projected temperature, effective area, and metallicity as a function of radius, we then convert the *Chandra* count rate in the 0.7–2.0 keV band into the emission integral, EI $= \int n_{\rm e} n_{\rm p} dV$, within each cylindrical shell. To compute the emission measure and temperature profiles we assume spherical symmetry, although the X-ray morphology of 4C+37.11 exhibits a mildly elliptical shape. The spherical assumption is expected to introduce only negligible (less than 3%) deviation (Piffaretti et al. 2003).

We then fit the emission measure profile assuming the gas density profile follows Vikhlinin et al. (2006):

$$n_{\rm e} n_{\rm p} = n_0^2 \frac{(r/r_{\rm c})^{-\alpha}}{(1+r^2/r_{\rm c}^2)^{3\beta-\alpha/2}} \frac{1}{(1+r^\gamma/r_{\rm s}^\gamma)^{\epsilon/\gamma}} + \frac{n_{02}^2}{(1+r^2/r_{\rm c2}^2)^{3\beta_2}}. \quad (1)$$

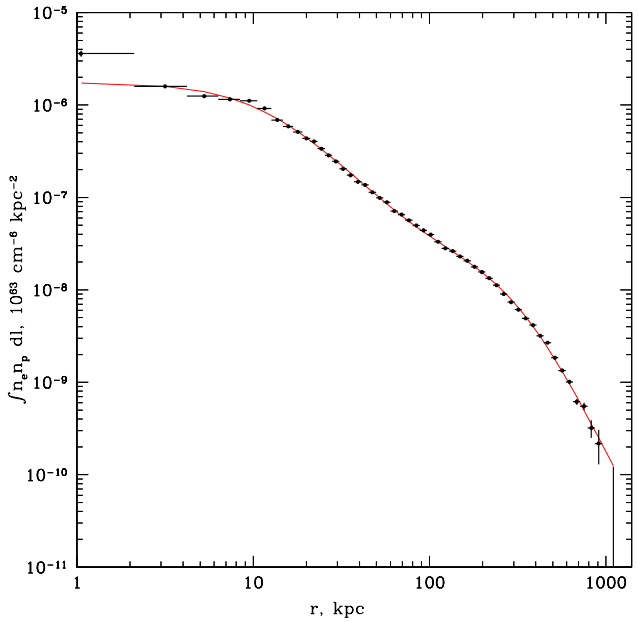

FIG. 1.— Observed projected emissivity profile for 4C+37.11. The solid line shows the emission measure integral of the best fit to the emissivity profile given by Equation (1). The emission from the nucleus is excluded from the fit, since it exhibits an enhanced emission due to the AGN.

This relation is based on a classic β-model, however it is modified to account for the power-law type cusp and the steeper emission measure slope at large radii. In addition a second β-model is included, giving extra freedom to characterize the cluster core. For further details on this equation we refer to Vikhlinin et al. (2006). The relation between the electron number density and gas mass density is given by $\rho_{\rm g} = \mu_{\rm e} n_{\rm e} m_{\rm a}$, where $m_{\rm a}$ is the atomic mass unit and $\mu_{\rm e}$ is the mean molecular weight per electron. For a typical metallicity of 0.3 $Z_\odot$, the reference values from Anders & Grevesse (1989) yields $\mu_{\rm e} = 1.17058$ and $n_{\rm e}/n_{\rm p} = 1.1995$.

The best fit parameters of Equation 1 are presented in Table 1.

3.2. *Gas Temperature Radial Profiles*

Most clusters present a temperature profile that has a broad peak within 0.1–0.2 r_{200}[1]. (Vikhlinin et al. 2006) presents a 3D temperature profile that describes these general features. At large radii, the temperature profile can be fairly represented as a broken power law with a transition region:

$$T(r) = \frac{(r/r_t)^{-a}}{(1+(r/r_t)^b)^{c/b}}. \quad (2)$$

At small radii, the temperature profile can be described as

$$T_{\rm cool}(r) = (x + T_{\rm min}/T_0)/(x+1), \quad (3)$$

where $x = (r/r_{\rm cool})^{a_{\rm cool}}$. The final analytical expression

[1] r_{200} and r_{500} are used to define a radius at the over-density of 200 and 500 times the critical density of the Universe at the cluster redshift, respectively.

TABLE 1
PARAMETERS FOR THE EMISSION MEASURE PROFILE (EQUATION 1)

n_0 (10^{-2} cm^{-3})	r_c (kpc)	r_s (kpc)	α	β	γ	ϵ	n_{02} (10^{-3} cm^{-3})	r_{c2} (kpc)	β_2
5.28 ± 0.62	11.7 ± 1.4	46.4 ± 3.8	0.02 ± 0.11	0.359 ± 0.027	0.94 ± 0.19	1.66 ± 0.37	1.425 ± 0.083	331 ± 18	0.935 ± 0.039

NOTE. — Columns list best fit values for the parameters given by Equation 1.

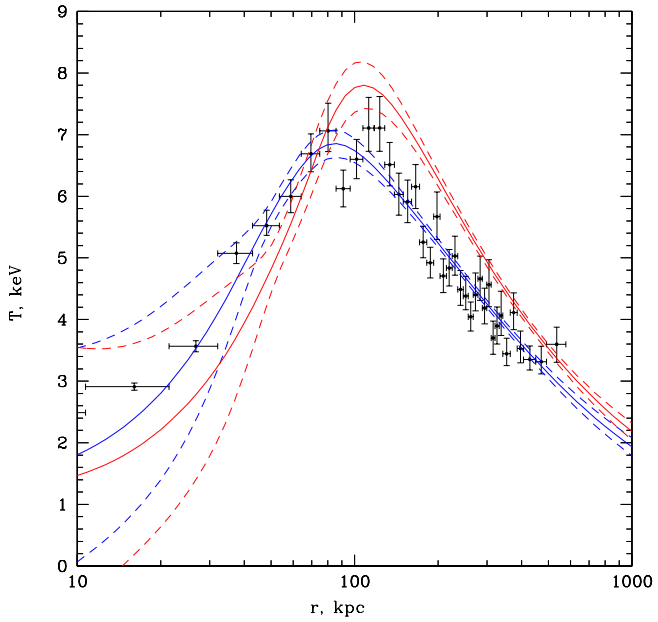

FIG. 2.— Azimuthally averaged, radial temperature profile. Observed projected temperatures are shown by points with error bars. The 3D model and its projected effective temperatures (the latter to be compared with the data) are shown by the red and blue curves, respectively. Dashed lines show the 1σ uncertainty ranges.

for the 3D temperature profile is,

$$T_{3D}(r) = T_0 \times T_{cool}(r) \times T(r). \quad (4)$$

This temperature model has significant functional freedom (8 parameters) and can adequately describe almost any smooth temperature distribution. Thus, we use this model, from Vikhlinin et al. (2006), to describe the temperature distribution of the hot gas in 4C+37.11.

To estimate the uncertainties in the best values for the parameters of this analytical model, we performed Monte-Carlo simulations. This model for $T_{3D}(r)$ (Equation 4) allows very steep temperature gradients. In some Monte-Carlo realizations, such profiles are mathematically consistent with the observed projected temperatures, however, large values of temperature gradients often lead to unphysical mass estimates, such as profiles with negative dark matter density at some radii. We solved this issue by accepting only Monte-Carlo realizations in which the best-fit temperature profile leads to $\rho_{tot} > \rho_{gas}$ in the radial range $r \leq 1.5 r_{500}$, where $\rho_{tot} = \rho_{gas} + \rho_{\text{dark matter}}$. Also, in the same radial range, we verified that the temperature profiles are all convectively stable, i.e. $d \ln T / d \ln \rho_g < 2/3$.

To construct the temperature profile, we extracted spectra from 38 annuli in the radial range from 0 to ~ 600 kpc and fit them with an absorbed `APEC` model. For the fitting we fixed the column density at $N_H = (8.2 \pm 0.4) \times 10^{21}$ cm^2. This value was obtained by fitting the central 500 kpc region of the cluster with an absorbed `APEC` model (with abundance fixed at $A = 0.3$ Solar) leaving the column density as a free parameter. This fit resulted in a best-fit temperature of $kT = 4.6 \pm 0.2$ keV and $N_H = (8.2 \pm 0.4) \times 10^{21}$ cm^2. This gives an equivalent $A_V = N_H/(2.2 \times 10^{21}$ cm$^2) = 3.7$, in excellent agreement with the full Galactic extinction estimated from the reddening maps (Schlegel et al. 1998; Green et al. 2015), suggesting that the intrinsic absorption is small. We then followed the procedures described above to obtain the 2D and 3D temperature profiles. The measured 2D (black data points), fitted 2D (blue solid line), and 3D (red solid line) temperature profiles are presented in Figure 2. The 2D temperature profile was computed by projecting the 3D temperature weighted by gas density squared using the spectroscopic-like temperature (Mazzotta et al. 2004, provides a formula for the temperature which matches the spectroscopically measured temperature within a few percent):

$$T_{2D} = T_{spec} \equiv \frac{\int \rho_g^2 T_{3D}^{1/4} dz}{\int \rho_g^2 T_{3D}^{-3/4} dz} \quad (5)$$

The best fit parameters of equations 2 and 3 are presented in Table 2.

3.3. *Total and Gas Masses*

Assuming hydrostatic equilibrium and using the three-dimensional analytical expressions for the temperature and gas density profiles, one can compute the total enclosed mass within a radius r with the following equation (e.g., Sarazin 1988):

$$M(r) = \frac{-kTr}{\mu m_H G} \left(\frac{d \ln \rho_g}{d \ln r} + \frac{d \ln T}{d \ln r} \right)$$
$$= -3.67 \times 10^{13}\ M_\odot kTr \left(\frac{d \ln \rho_g}{d \ln r} + \frac{d \ln T}{d \ln r} \right), \quad (6)$$

where T is the temperature in units of K, k is the Boltzmann constant, and r is in units of Mpc. The normalization corresponds to $\mu = 0.6107$, which was computed for an abundance of 0.3 $Z_\odot$.

Using Equation 6, r_{500} is directly computed by solving

$$M(r_{500}) = 500 \rho_c (4\pi/3) r_{500}^3, \quad (7)$$

where ρ_c is the critical density of the Universe at the cluster redshift. Using Equations 6 and 7, we obtain $r_{500} = 945^{+21}_{-22}$ kpc and a corresponding hydrostatic mass of $M_{500,hyd} = (2.53 \pm 0.17) \times 10^{14} M_\odot$ (Figure 3).

Using the best fit parameters for the density profile (see Table 1), we compute a gas mass within r_{500} of $M_{g,500} =$

TABLE 2
Parameters for the Temperature Profile (Equations 2 and 3)

T_0 (keV)	$T_{\rm min}$ (keV)	$r_{\rm t}$ (kpc)	$r_{\rm cool}$ (kpc)	$a_{\rm cool}$	a	b	c
37 ± 37	14.2 ± 7.7	75 ± 58	97 ± 100	4.8 ± 3.4	-2.1 ± 3.2	3.1 ± 1.9	2.9 ± 2.4

Note. — Columns list best fit values for the parameters given by Equations 2 and 3.

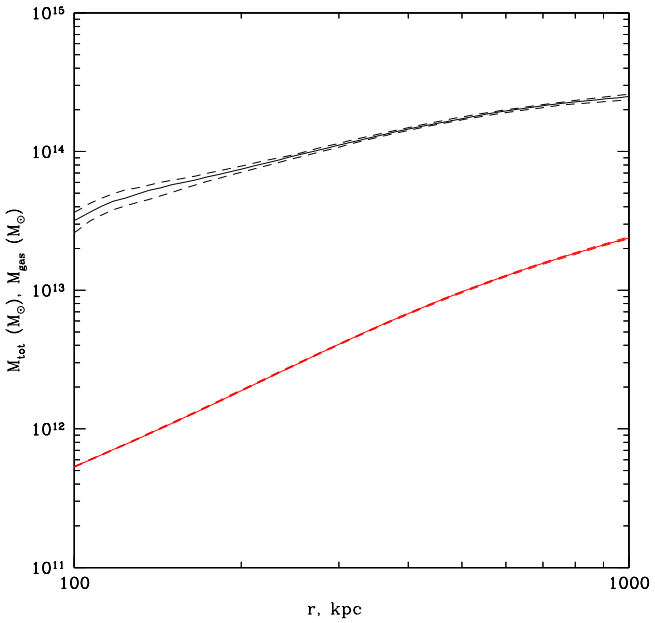

Fig. 3.— Computed mass profiles. Black and red lines correspond to total and gas mass profiles, respectively. Dashed lines correspond to 68% confidence range.

$(2.24 \pm 0.06) \times 10^{13} M_\odot$. The gas mass fraction within r_{500} is $f_{\rm g} = 0.09 \pm 0.01$ and is in agreement with the expected value (see Fig. 21 from Vikhlinin et al. 2006) for clusters with $kT \sim 4.5$ keV ($f_{\rm g} \sim 0.09$–0.10). The results are summarized in Table 3.

3.4. *Entropy Profiles*

The intracluster gas entropy index is defined as

$$K = \frac{kT}{n_{\rm e}^{2/3}}, \quad (8)$$

where $n_{\rm e}$ is the electron density, T is the gas temperature, and k is the Boltzmann constant. The entropy index is directly related to the thermodynamic history of the ICM. The entropy index increases when heat energy is deposited non-adiabatically into the ICM, and decreases when radiative cooling carries heat energy away (Voit et al. 2005). To understand the thermodynamic history of the halo hosting 4C+37.11, we computed entropy profiles, which are presented in Figure 4.

Departure from the self-similar scaling relation $K/K_{500} = 1.42(r/r_{500})^{1.1}$ (Pratt et al. 2010) is suggestive of non-gravitational processes, where K_{500} is computed by:

$$K_{500} = 106 \text{ keVcm}^2 \left(\frac{M_{500}}{10^{14} h_{70}^{-1} M_\odot}\right)^{2/3} \left(\frac{1}{f_{\rm b}}\right)^{2/3} \times E(z)^{-2/3} h_{70}^{-4/3}, \quad (9)$$

where $f_{\rm b} = 0.15$ is the baryon fraction and $E(z) = (\Omega_{\rm M}(1+z)^3 + \Omega_{\rm k}(1+z)^2 + \Omega_\Lambda)^{1/2}$. Figure 4 shows the dimensionless entropy profile of the galaxy halo hosting 4C+37.11. We see that the entropy index is higher, at all radii than the scaling relation $K/K_{500} = 1.42(r/r_{500})^{1.1}$, which suggests that non-gravitational processes are playing a significant role in the thermodynamics of the ICM, even at large distances from the center of the cluster. We see substantial energy injection in the center of the cluster extending several arcmin, to $\sim 0.3 r_{500}$. Note that this is well outside of the $\sim 10''$ radius of the radio lobes currently being inflated by the nucleus, so it is not the direct product of the current AGN activity (Section 5). This entropy excess is suppressed by core cooling within ~ 100 kpc, which returns the entropy close to the Pratt et al. (2010) scaling set by K_{500} at large radius.

4. RESULTS

4.1. *Images*

The left panel of Figure 5 shows the merged, flat-fielded (vignetting and exposure corrected), and background subtracted $0.5 - 2$ keV band *Chandra* ACIS-I image of 4C+37.11. The image, depicting the inner 960×960 kpc region of the cluster, reveals the presence of large scale diffuse emission, which originates from optically-thin thermal plasma with $kT \sim 3 - 7$ keV temperature (Section 3).

The distribution of the hot X-ray emitting gas reveals a complex morphology, indicating an active merger history. In particular, the gas distribution is not symmetric, but is elongated in the east-west direction. In addition, the image shows the presence of sharp surface brightness edges in the central regions of the cluster. To further investigate the surface brightness features in the central regions of the cluster, we show a zoomed-in version of the large-scale image in the right panel of Figure 5. This image depicts the central 128×128 kpc region of 4C+37.11, and confirms our findings. Indeed, the hot gas distribution exhibits asymmetry at scales of 10 kpc, and hints at the presence of sharp surface brightness edges.

The above features are characteristic signatures of a merger, which has likely perturbed the hot gas distribution. To explore the nature of these features, and hence, constrain the merger history of the cluster, we derive surface brightness, density, and temperature profiles, which are discussed in the following sections.

4.2. *Profiles*

In galaxy clusters, sharp surface brightness edges may be caused by three phenomena: cold fronts induced by mergers, sloshing of the gas in the central regions of clusters induced by minor mergers, and shocks associated with mergers and supersonic inflation of radio lobes.

TABLE 3
Physical Properties Derived Assuming Hydrostatic Equilibrium

r_{500} (kpc)	$M_{g,500}$ (10^{13} $M_\odot$)	M_{500} (10^{14} $M_\odot$)	f_g	kT (keV)	L_X (10^{44} erg s^{-1})
945^{+21}_{-22}	2.24 ± 0.06	2.53 ± 0.17	0.09 ± 0.01	4.6 ± 0.2	1.10 ± 0.01

Note. — Columns list the cluster r_{500}, gas mass, total mass derived from the hydrostatic equilibrium equation (Equation (6)), gas fraction, spectroscopic-like temperature, and bolometric X-ray luminosity within r_{500}.

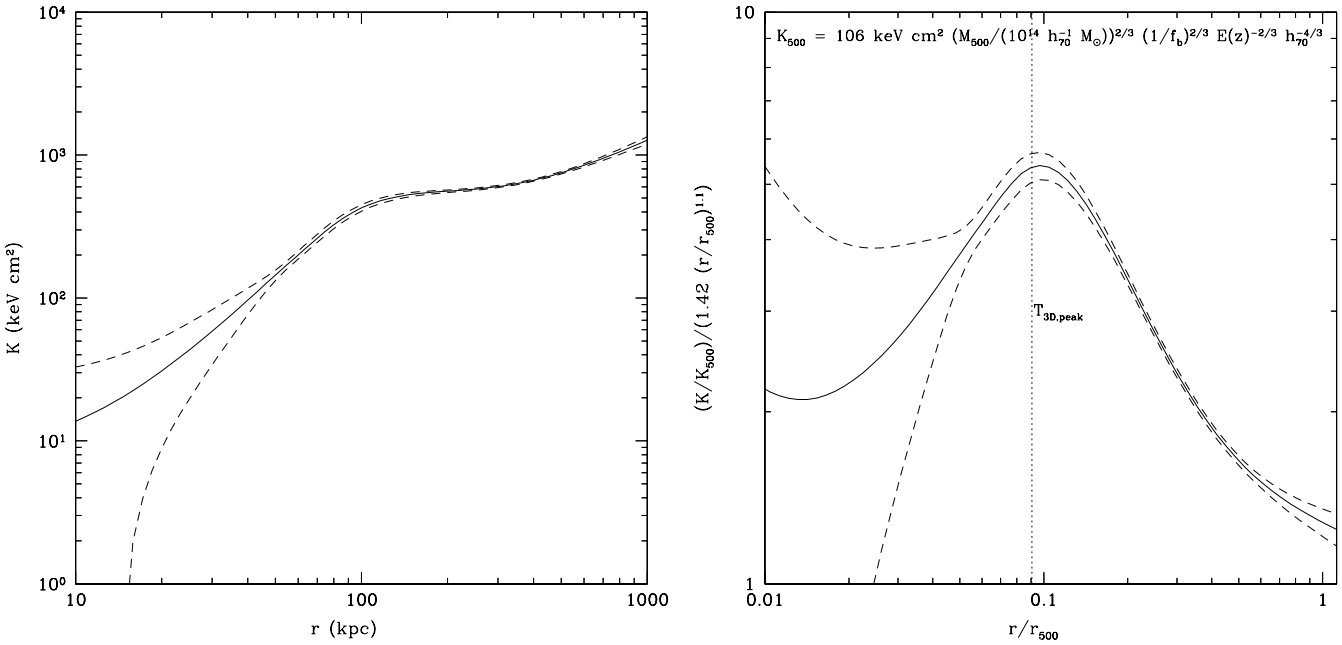

Fig. 4.— Left: Entropy profile of the halo hosting 4C+37.11. Right: Dimensionless entropy profile of 4C+37.11. We see that the entropy index is higher at all radii than the scaling relation $K/K_{500} = 1.42(r/r_{500})^{1.1}$, which suggests that non-gravitational processes are playing a significant role in the thermodynamics of the ICM even at large distances from the center of the cluster. Dashed lines correspond to 68% confidence ranges.

To probe the origin of the surface brightness edges in 4C+37.11, we build surface brightness, density, and temperature profiles, and derive the pressure jump across the edges. If the edges originate from a major sub-cluster merger, a temperature and pressure jump is expected across the surface brightness discontinuity. If, however, the edge is due to sloshing, we expect to detect a change in the temperature and density across the edge, but the pressure should remain at or near equilibrium.

To construct the surface brightness profiles, we extracted the brightness in circular wedge regions towards many sectors using `PROFFIT`, an interactive software for the analysis of X-ray surface brightness profiles (Eckert et al. 2011). Two of them presented surface brightness discontinuities: the northwest (position angles $0° - 45°$) and southeast ($210° - 255°$) of the cluster – the locations of these regions are shown in the right panel of Figure 5. The background subtracted $0.5 - 2$ keV band profiles are depicted in the top panels in Figure 6. The profiles demonstrate the presence of surface brightness jumps, which are located at $\sim 34''$ and $\sim 51''$ central distance on the northwest and southeast, respectively. To constrain the jump conditions, we fit the surface brightness profile within each wedge assuming spherical symmetry for the gas density and constant gas temperature. The density profile is assumed to follow a β-model and a power law, which is given by the following equations:

$$n(r) = \begin{cases} A\left[1 + (r/r_c)^2\right]^{-3\beta/2}, & r \le r_{cut} \\ B\,(r/r_c)^{-\alpha}, & r > r_{cut} \end{cases} \quad (10)$$

where r_c is the core radius, and r_{cut} is the radius where the density abruptly changes. The constants A and B are related by:

$$B = \frac{A\left[1 + (r_{cut}/r_c)^2\right]^{-3\beta/2}}{C\,(r_{cut}/r_c)^{-\alpha}} \quad (11)$$

where C is the density jump.

The best-fit density profiles are shown in the bottom panels in Figure 6. These profiles reveal density jumps of $1.60^{+0.29}_{-0.20}$ and $1.66^{+0.15}_{-0.15}$ for the northwest and southeast regions of the cluster, respectively (Table 4). In addition, the position of the jumps are strongly asymmetric between the two sides of the cluster, since they are at $34''$ on the northwest and at $51''$ on the southeast. The best-fit parameters of the fits are listed in Table 4.

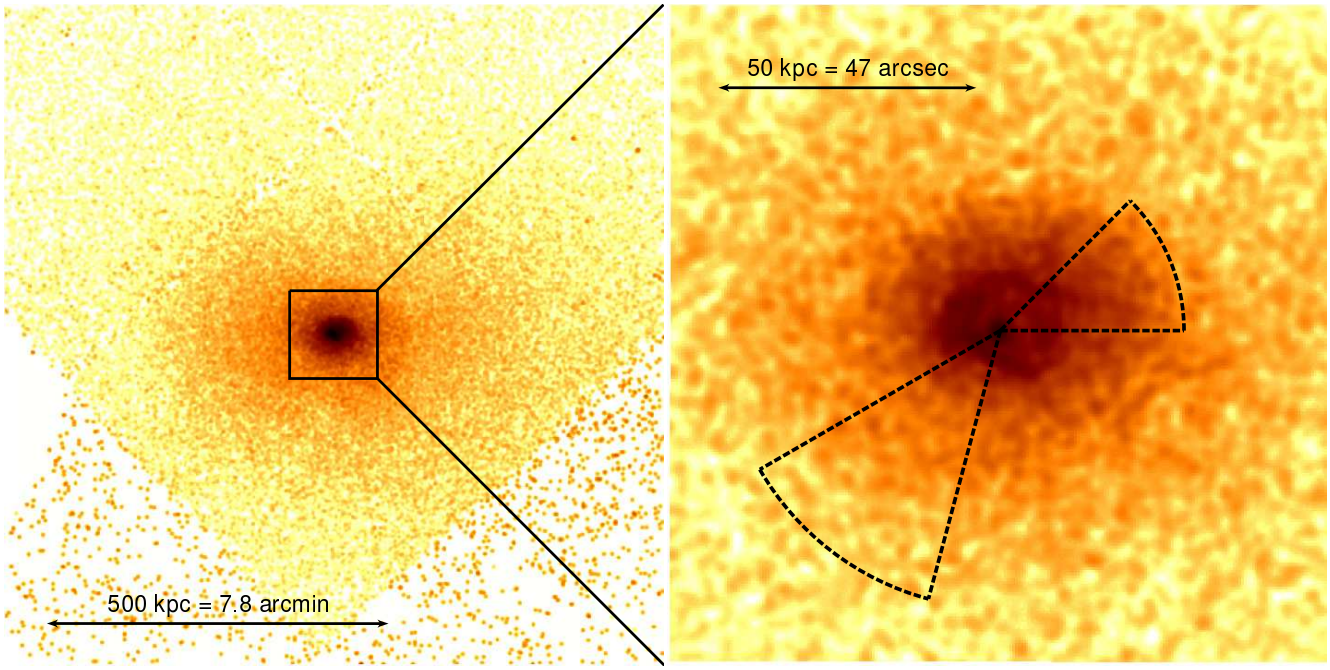

FIG. 5.— The left panel shows the 0.5 − 2 keV band merged *Chandra* image of a $15' \times 15'$ (960×960 kpc) region of 4C+37.11. To highlight the large-scale features in the hot gas distribution, the image was smoothed with a Gaussian kernel of two-pixel size. Bright point sources have been excluded and their location has been filled with the local background level. The box shows a $2' \times 2'$ (128×128 kpc) region, which is depicted in the right panel. To make the small-scale features more pronounced, this image was smoothed with a Gaussian kernel of one-pixel size. The over plotted regions show the location and position angle of the wedge regions that were used to extract surface brightness and density profiles. The outer shell of the regions marks the position of the surface brightness edges, which are detected with the surface brightness profiles in Figure 6. Note that the positions of the surface brightness jumps are azimuthally asymmetric.

TABLE 4
THE BEST-FIT JUMP CONDITIONS

	Northwest	Southeast
β	0.35 ± 0.17	0.37 ± 0.05
α	1.07 ± 0.05	0.85 ± 0.10
r_c [$'$]	0.21 ± 0.16	0.11 ± 0.07
r_{cut} [$''$]	34 ± 1	51 ± 1
$n_{0,cut}/n_{1,cut}$	$1.60^{+0.29}_{-0.20}$	1.66 ± 0.15
$T_{0,cut}/T_{1,cut}$	0.55 ± 0.05	0.46 ± 0.08
$p_{0,cut}/p_{1,cut}$	0.88 ± 0.18	0.76 ± 0.15

To probe the presence of temperature jumps associated with the density jumps, we extract X-ray energy spectra wedges using wedges with position angles of $0° - 45°$ and $210° - 255°$ for the northwest and southeast regions, respectively. The width of the regions was $17''$ for the northwest and $25''$ for the southeast regions, with the boundary positioned at the expected location of the jump. The spectra are fit with an optically-thin thermal plasma emission model (APEC in XSPEC). We have fixed the column density at $N_H = 8.2 \times 10^{21} cm^{-2}$ and the metal abundances at $A = 0.3$ (Section 3.2). For the northwest of the cluster we measure $T_{0,cut} = 2.64^{+0.12}_{-0.09}$ keV and $T_1 = 4.84^{+0.36}_{-0.35}$ keV, while for the southeast we obtain $T_0 = 3.95^{+0.21}_{-0.20}$ keV and $T_1 = 8.66^{+1.37}_{-1.15}$ keV. Thus, we obtain a statistically significant temperature jump on both sides of the cluster with temperature jumps of $T_0/T_1 = 0.55 \pm 0.05$ and $T_0/T_1 = 0.46 \pm 0.08$ for the northwest and southeast, respectively.

Based on these data we compare the pressures on both sides of the surface brightness jumps using $p = n_e kT$, where n_e is the electron density and kT is the gas temperature. The derived pressure ratios of $p_0/p_1 = 0.88 \pm 0.18$ for the jump located on the West, and $p_0/p_1 = 0.76 \pm 0.15$ for the jump at the East, where p_0 and p_1 correspond to the pressures within and beyond the jumps, respectively.

Thus, the hot gas is in approximate pressure equilibrium, implying that the observed sharp surface brightness edges most likely originate from the sloshing of the hot gas (Markevitch & Vikhlinin 2007).

4.3. *Spiral pattern of the hot gas*

The telltale sign of gas sloshing is the presence of a spiral structure in the hot gas distribution (Markevitch & Vikhlinin 2007). However, the presence of such underlying features may not be apparent in the X-ray images due to the strong surface brightness gradient associated with the cluster. Therefore, we have produced a "residual" X-ray image, in which the merged, flat-fielded, and background subtracted 0.5 − 2 keV band X-ray image was divided by an azimuthally averaged X-ray image. Note that we excluded bright point sources and filled their locations with local background. To construct the azimuthally averaged image, we described the surface brightness of the cluster with an elliptical β-model, and produced the average image according to the best-fit properties of this model. Finally, the residual image was smoothed with a Gaussian with a kernel size of $\sim 2''$. The residual ratio image removes the strong surface brightness gradients, allowing us to explore faint underlying features.

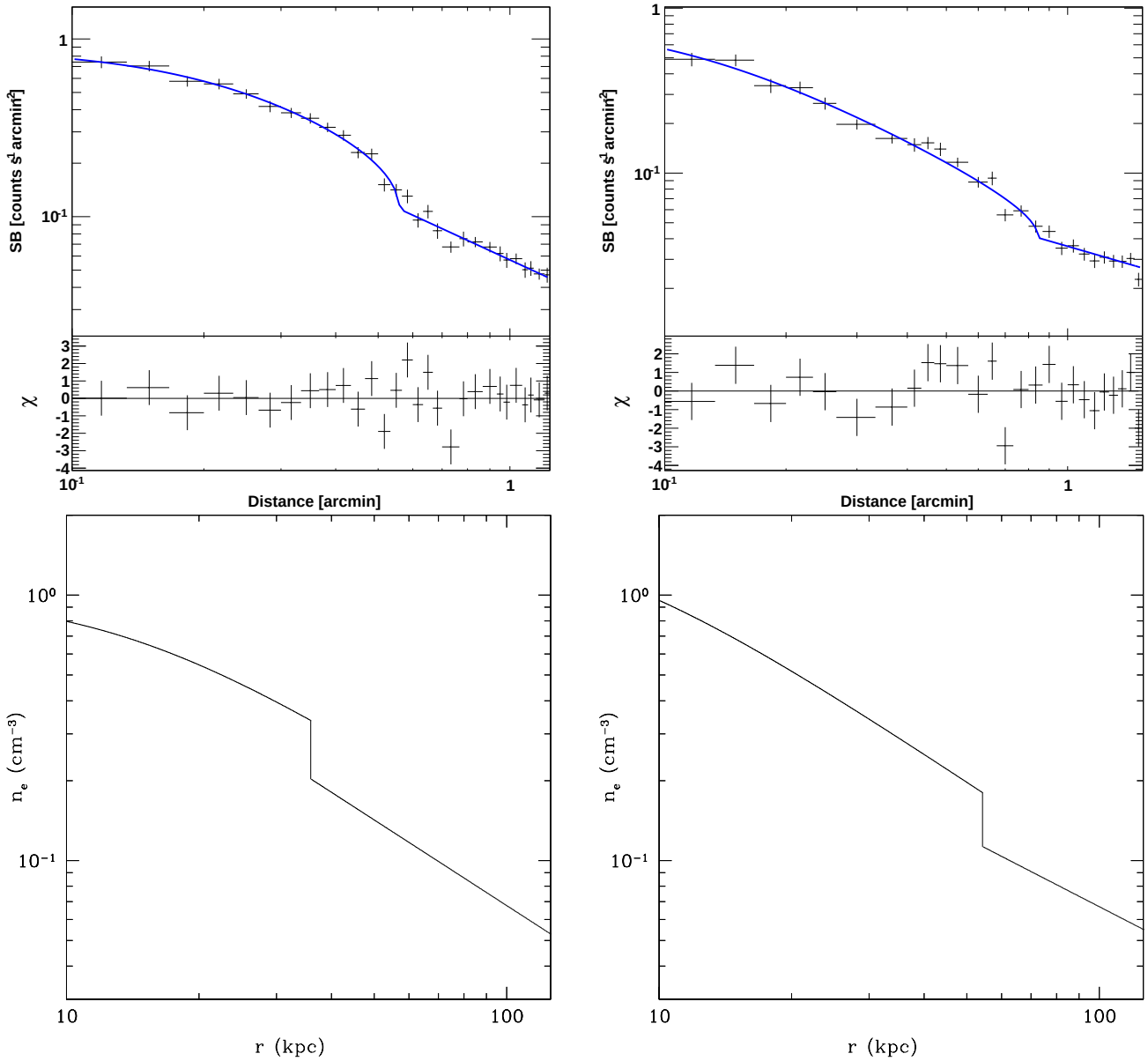

FIG. 6.— Surface brightness (top panels) and deprojected density (bottom panels) profiles of the central regions of 4C+37.11 for the position angles $0^\circ - 45^\circ$ (left) and $210^\circ - 255^\circ$ (right). Note that position angle 0° is towards the West. The regions that were used to construct the profiles are depicted in the right panel of Figure 5. The solid line shows the best fit model to the profiles, which is composed of a β-model and power law. Note the presence of the jump in surface brightness and density at $34''$ and $51''$ for the $0^\circ - 45^\circ$ and $210^\circ - 255^\circ$ wedges, respectively.

The residual image, shown in the left panel of Figure 7, hints at the presence of a spiral pattern in the central regions of the cluster. Indeed, this feature is very similar to that obtained in other clusters, such as the Perseus cluster (Churazov et al. 2003). To directly compare the spiral structure observed in 4C+37.11 and sloshing feature observed in Perseus, we compare their images side-by-side in Figure 7 at the same physical scale. These images share a number of similar features, such as the bright knot in the center, the excess emission on the eastern side of the knot and the fainted emission on the northern side of the spiral pattern. Overall, the residual image supports our earlier findings based on the pressure profiles, and hints that the hot gas of 4C+37.11 is sloshing. Indeed the overall similarity of scale and structure to that seen in Perseus suggests a similar time since the last merger event.

5. SMALL SCALE STRUCTURE

In galaxies, galaxy groups, and galaxy clusters, cavities in the hot gas distribution are widely observed, and hint at the presence of AGN outbursts. Indeed, powerful radio sources are capable of drastically increasing the entropy of the hot gas, inflating the gas distribution and reducing its density.

Radio observations of 4C+37.11 point at the existence of radio lobes in the central $20''$ region of the host elliptical. In Figure 8, we show the $0.5 - 2$ keV band merged *Chandra* X-ray image of the cluster along with the intensity levels of the 1.4 GHz VLA data. Interestingly, the

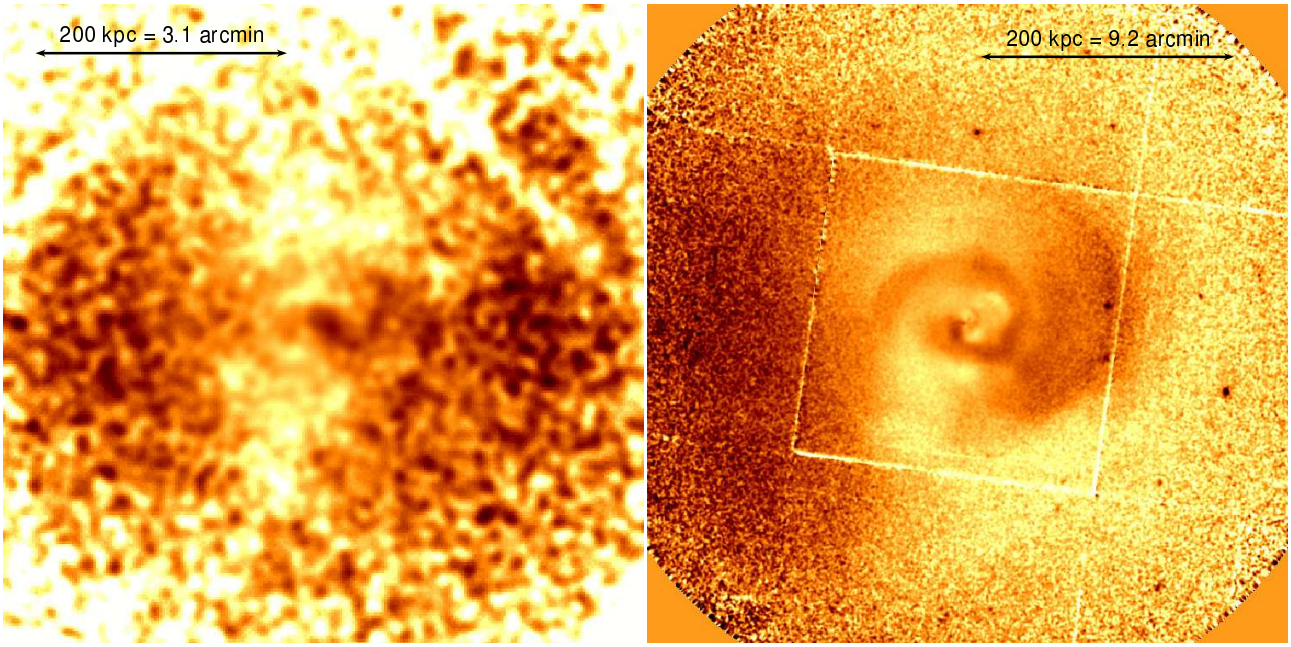

FIG. 7.— Left: The residual $0.5-2$ keV band *Chandra* image of 4C+37.11 showing the underlying structure of the hot gas. To produce this image, we divided the merged X-ray image with an azimuthally averaged image. To enhance the features, the image was smoothed with a Gaussian with a kernel size of 4 pixels. Point sources were excluded and their location were filled with the local emission level. The residual image hints at the presence of a spiral-like feature, which is the characteristic signature of sloshing. Right: The sloshing pattern of Perseus cluster taken from (Churazov et al. 2003). Note the similar features between the two clusters. Both images depict the same physical regions on the sky. Both clusters show the presence of a knot in the central regions, the excess X-ray emission in the eastern side, and the spiral pattern of the hot gas. Note that the spiral pattern is more graphic in the Perseus cluster, which is due to its proximity and the significantly deeper X-ray observations.

X-ray image of 4C+37.11 (see Figure 8) hints that at the position of the radio lobes a decrement in the X-ray surface brightness may be present. While the distribution of the hot X-ray gas exhibits strong asymmetries, the decrements in the X-ray surface brightness are not exactly associated with the position of the radio lobes. To quantitatively probe the possible anti-correlation between the X-ray and radio intensity levels, we extract the $0.5-2$ keV band X-ray and 1.4 GHz radio surface brightness profiles in annular wedges. The profile, shown in the right panel of Figure 8, shows that there is no clear anti-correlation between the X-ray and radio surface brightness, which is confirmed by a two sample Kolmogorov-Smirnov test between the X-ray and reciprocal radio fluxes that excludes similarity at $p = 2.05 \times 10^{-5}$. However, a weak anti-correlation might be suppressed by projection effects.

6. DISCUSSION

The detection of likely sloshing features in the X-ray halo of 4C+37.11 allows us to place constraints on the interaction which created these structures. While the presence of the radio outflow associated with the CSO raises the possibility that AGN-driven bubbles can affect the inner halo structure, the presence of edges at large radius and the overall spiral appearance of the residual image (Figure 7) makes it likely that a dynamical interaction has defined the basic disturbance. Further, given the marked similarity to the Perseus halo, it is productive to compare with the simulations of Ascasibar & Markevitch (2006) and ZuHone et al. (2010). These simulations assume a 1:5 merger mass ratio and impact parameter b = 500 kpc and result in spiral gas distribution matching that seen in Perseus at times $1-2$ Gyrs after the first passage of the interacting sub-cluster. At this time this sub-cluster makes its second approach, but the cores have not yet merged. The stellar component of such a sub-cluster for 4C+37.11 is not obvious; it might be identified with the nearest, 2.5 mag fainter, galaxy about $25''$ (~ 27 kpc) projected distance away or with a more distant object, but kinematic studies are needed to test such association.

We next consider the implications for the unique tight double radio nucleus of this source. Recalling that VLBI studies of over 3000 AGN have found no other resolved < 10 pc-scale system (Burke-Spolaor 2011) , it is important to consider whether other unusual system properties (such as the bright X-ray halo) can inform us about the nucleus. The rarity of resolved double nuclei implies a short < 0.5 Gyr time between galaxy core merger and GR-driven inspiral (Burke-Spolaor 2011). In turn this implies that some source other than dynamical friction drives the BH cores to radii where GR can take over. So we must ask: why is 4C+37.11 seen at 7pc projected separation?

Broadly speaking there are two possibilities. Perhaps we are simply catching this binary shortly after core merger when the black holes are still approaching each other. Alternatively, the typically dominant merger mechanism (likely mediated by interactions with dissipative circumbinary gas) is under-performing in 4C+37.11, leaving it stalled at resolvable scale. At face value the presence of large scale sloshing structures eliminates the first possibility. Here we adopt the $\sim 1-2$ Gyrs time scale since the last major interaction implied by the spiral morphology and we note that the cores of the galaxies

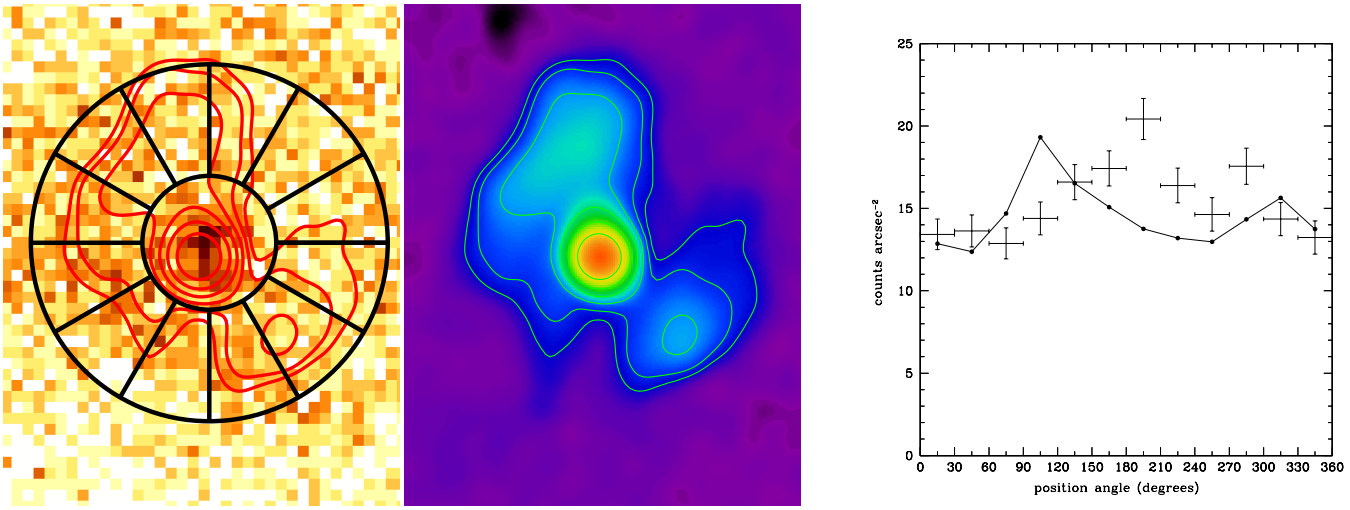

FIG. 8.— Left: $0.5-2$ keV band merged *Chandra* X-ray image of the central $17'' \times 22''$ region of 4C+37.11. Overlayed are the intensity levels of the 1.4 GHz VLA observations. Note that the intensity levels are spaced logarithmically. There is no clear correlation between the decrements in the X-ray surface brightness distribution and the position of the radio lobes. Right: X-ray and radio surface brightness profiles extracted from circular wedges with $3''-8''$ radii. Points with error bars represent the X-ray surface brightness, while the connected points show the radio intensity levels, which were arbitrarily normalized to match the X-ray surface brightness level. The position angle 0° is toward the West. Note the absence of an anti-correlation between the X-ray and radio intensity levels.

in this interaction should remain unmerged. Thus the interaction of the two cores contributing the observed, resolved supermassive black hole binary must have occurred even earlier, implying that these holes have remained unmerged for several Gyr. This is substantially longer than the bounds on typical merger timescale.

We see that our X-ray halo studies, while not directly probing at the black hole binary scale, have allowed us to conclude that unusual core properties must exist in 4C+37.11, permitting the black hole to languish at < 10 pc separation for several Gyrs. Dynamical studies of the core, and especially studies of the atomic and molecular gas will be helpful in directly exploring conditions in the circumbinary environment.

7. CONCLUSIONS

We present results from *Chandra* observations of the cluster-scale X-ray halo surrounding 4C+37.11, a nearby (z=0.055) galaxy that hosts the closest known resolved supermassive black hole binary. We derive within r_{500} a total mass of $M_{500} = (2.5 \pm 0.2) \times 10^{14}$ M$_\odot$, a gas mass of $M_{g,500} = (2.2 \pm 0.1) \times 10^{13}$ M$_\odot$ an X-ray bolometric luminosity of $L_{bol,500} = (1.10 \pm 0.01) \times 10^{44}$ erg s^{-1}, and a temperature of $kT = 4.6 \pm 0.2$ keV. The gas mass fraction within r_{500} is $f_g = 0.09 \pm 0.01$, in agreement with the expected value, given the cluster temperature. We present total mass, gas mass, and entropy profiles. Evidence of gas sloshing comes from extraction of surface brightness and temperature profiles in selected wedges, where we show that despite the density jump, the pressure is continuous along the contact discontinuities. We conclude that the host of the radio galaxy 4C+37.11 is probably a relaxed fossil cool-core cluster that has been mildly disturbed as a smaller group or cluster interacted gravitationally during close approach and "sloshed" the cool gas residing at its center. The interaction driving the sloshing appears to have occurred $1-2$ Gyrs ago, while the interaction producing the binary black hole nucleus occurred even earlier. This allows us to conclude that the supermassive black hole binary in 4C+37.11 is not young and has stalled outside the present orbital separation for several Gyrs, longer than the time scale inferred for typical black hole binary coalescence.

The authors thank Eugene Churazov for kindly providing the Perseus residual image, Maxim Markevitch for helpful discussions, and Alexey Vikhlinin and Georgiana Ogrean for providing software. F.A-S. acknowledges support from *Chandra* grant G03-14131X. Á.B., W.R.F., C.J. are supported by the Smithsonian Institution. R.W.R was supported in part by NASA grant G04-15116A.

REFERENCES

Anders, E., & Grevesse, N. 1989, Geochim. Cosmochim. Acta, 53, 197
Andrade-Santos, F., Lima Neto, G. B., & Laganá, T. F. 2012, ApJ, 746, 139
Andrade-Santos, F., Nulsen, P. E. J., Kraft, R. P., et al. 2013, ApJ, 766, 107
Arnaud, M., Pratt, G. W., Piffaretti, R., et al. 2010, A&A, 517, A92
Ascasibar, Y., & Markevitch, M. 2006, ApJ, 650, 102
Beers, T. C., Flynn, K., & Gebhardt, K. 1990, AJ, 100, 32
Beers, T. C., Gebhardt, K., Huchra, J. P., et al. 1992, ApJ, 400, 410
Begelman, M. C., Blandford, R. D., & Rees, M. J. 1980, Nature, 287, 307
Bell, E. F., McIntosh, D. H., Katz, N., & Weinberg, M. D. 2003, ApJS, 149, 289
Bell, E. F., Phleps, S., Somerville, R. S., et al. 2006, ApJ, 652, 270
Bock, D. C.-J., Large, M. I., & Sadler, E. M. 1999, AJ, 117, 1578
Burke-Spolaor, S. 2011, MNRAS, 410, 2113
Churazov, E., Forman, W., Jones, C., Böhringer, H. 2003, ApJ, 590, 225
Douglass, E. M., Blanton, E. L., Clarke, T. E., Randall, S. W., & Wing, J. D. 2011, ApJ, 743, 199
Eckert, D., Molendi, S., & Paltani, S. 2011, A&A, 526, A79
Eracleous, M., Boroson, T. A., Halpern, J. P., & Liu, J. 2012, ApJS, 201, 23
Forman, W., & Jones, C. 1982, ARA&A, 20, 547
Green, G. M., Schlafly, E. F., Finkbeiner, D. P., et al. 2015, ApJ, 810, 25
Graham, M. J., Djorgovski, S. G., Stern, D., et al. 2015, Nature, 518, 74
Jones, C., & Forman, W. 1984, ApJ, 276, 38
Jones, C., & Forman, W. 1999, ApJ, 511, 65
Kahn, F. D., & Woltjer, L. 1959, ApJ, 130, 705
Komossa, S., Burwitz, V., Hasinger, G., et al. 2003, ApJ, 582, L15
Laganá, T. F., Andrade-Santos, F., & Lima Neto, G. B. 2010, A&A, 511, A15
Li, Y.-S., & White, S. D. M. 2008, MNRAS, 384, 1459
Maness, H. L., Taylor, G. B., Zavala, R. T., Peck, A. B., & Pollack, L. K. 2004, ApJ, 602, 123
Markevitch, M. & Vikhlinin, A. 2007, Physics Reports, 443, 1
Mazzotta, P., Rasia, E., Moscardini, L., & Tormen, G. 2004, MNRAS, 354, 10
McDonald, M., Benson, B. A., Vikhlinin, A., et al. 2013, ApJ, 774, 23
Owen, F. N., O'Dea, C. P., Inoue, M., & Eilek, J. A. 1985, ApJ, 294, L85
Piffaretti, R., Jetzer, P., & Schindler, S. 2003, A&A, 398, 41
Rodriguez, C., Taylor, G. B., Zavala, R. T., et al. 2006, ApJ, 646, 49
Roediger, E., Lovisari, L., Dupke, R., et al. 2012, MNRAS, 420, 3632
Paterno-Mahler, R., Blanton, E. L., Randall, S. W., & Clarke, T. E. 2013, ApJ, 773, 114
Pratt, G. W., Arnaud, M., Piffaretti, R., et al. 2010, A&A, 511, A85
Romani, R. W., Forman, W. R., Jones, C., et al. 2014, ApJ, 780, 149
Schlegel, D. J., Finkbeiner, D. P., & Davis, M. 1998, ApJ, 500, 525
Seigar, M. S., Lynam, P. D., & Chorney, N. E. 2003, MNRAS, 344, 110
Smith, R. J., Hudson, M. J., Nelan, J. E., et al. 2004, AJ, 128, 1558
Vikhlinin, A., Markevitch, M., Forman, W., & Jones, C. 2001, ApJ, 555, L87
Vikhlinin, A., Markevitch, M., Murray, S. S., et al. 2005, ApJ, 628, 655
Vikhlinin, A., Kravtsov, A., Forman, W., et al. 2006, ApJ, 640, 691
Voit, G. M., Kay, S. T., & Bryan, G. L. 2005, MNRAS, 364, 909
Yan, C.-S., Lu, Y., Dai, X., & Yu, Q. 2015, ApJ, 809, 117
ZuHone, J. A., Markevitch, M., & Johnson, R. E. 2010, ApJ, 717, 908